6-2016

Mononuclear Iron-(hydro/semi)quinonate Complexes Featuring Neutral and Charged Scorpionates: Synthetic Models of Intermediates in the Hydroquinone Dioxygenase Mechanism

Amanda E. Baum
Marquette University, amanda.baum@marquette.edu

Sergey V. Lindeman
Marquette University, sergey.lindeman@marquette.edu

Adam T. Fiedler
Marquette University, adam.fiedler@marquette.edu

European Journal of Inorganic Chemistry : Special Issue: The Significance of Scorpionate Ligands 50 Years On (Cluster Issue), Vol. 2016, No. 15-16 (June 2016): 2455-2464. DOI.

Mononuclear Iron-(hydro/semi)quinonate Complexes Featuring Neutral and Charged Scorpionates: Synthetic Models of Intermediates in the Hydroquinone Dioxygenase Mechanism

Amanda E. Baum
Department of Chemistry, Marquette University, Milwaukee, WI
Sergey V. Lindeman
Department of Chemistry, Marquette University, Milwaukee, WI
Adam T. Fiedler
Department of Chemistry, Marquette University, Milwaukee, WI

Abstract

Neutral and anionic scorpionate ligands have been employed to generate active-site models of hydroquinone dioxygenases (HQDOs). While the nonheme Fe center in nearly all HQDOs is coordinated to one Asp (or Glu) and two His residues, 1,2-gentisate dioxygenase (GDO) is unique in featuring a three His triad instead. A synthetic GDO model was therefore prepared with the neutral tris(4,5-diphenyl-1-methylimidazol-2-yl)phosphine (^{Ph2}TIP) ligand. The gentisate substrate was mimicked with the bidentate ligand 2-(1-methylbenzimidazol-2-yl)hydroquinonate (BIHQ). X-ray diffraction analysis of the resulting complex, [Fe(^{Ph2}TIP)(BIHQ)]OTf (**1a**), revealed a distorted square-pyramidal geometry. Structural and electrochemical data collected for **1a** were compared to those previously reported for [Fe(^{Ph2}Tp)(BIHQ)] (**1b**), which features an anionic hydridotris(3,5-diphenylpyrazol-1-yl)borate (^{Ph2}Tp) ligand. Oxidation of **1a** and **1b** provides the corresponding Fe^{III} complexes (**2a**/**2b**) and the crystal structure of **2b** is reported. Both complexes undergo reversible deprotonation to yield the brown chromophores, **3a** and **3b**. Detailed studies of **3a** and **3b** with spectroscopic (UV/Vis absorption, EPR, resonance Raman) and computational methods determined that each complex consists of a high-spin Fe^{II} center ferromagnetically coupled to a *p*-semiquinonate radical (BISQ). The (de)protonation-induced valence tautomerization described here resembles key steps in the putative HQDO mechanism.

Abstract

Both neutral and anionic scorpionates are used to prepare synthetic models of hydroquinone dioxygenases (HQDOs) – a class of mononuclear nonheme enzymes. The different ligands mimic variations in coordination geometry within the HQDO family. The ferric-hydroquinonate complexes undergo reversible deprotonation to yield ferrous-semiquinonate species.

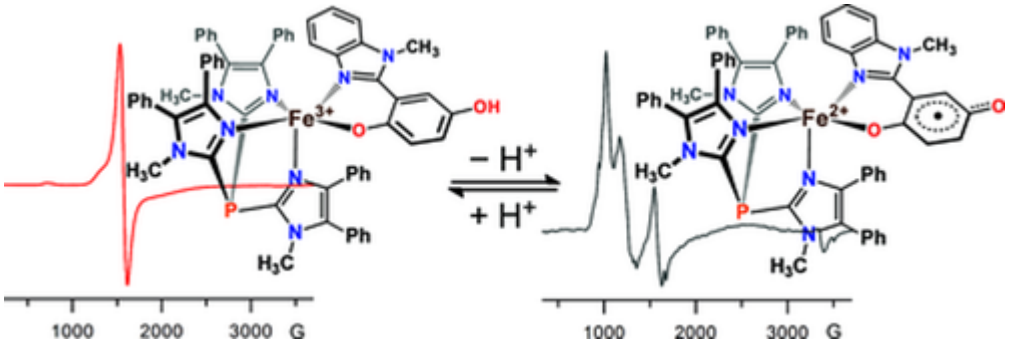

I. Introduction

The facially capping ligands known as “scorpionates” have been applied to nearly every aspect of coordination chemistry, including the preparation of synthetic metalloenzyme models.**1** Lippard and co-workers were the first to harness the biomimetic potential of this ligand family when they modeled the diiron active site of hemerythrin using Trofimenko's original scorpionate, hydridotris(pyrazol-1-yl)borate {Tp = $[HB(pz)_3]^-$}.**2** Soon thereafter, the emergence of second-generation ^{R}Tp ligands**3** featuring an alkyl or aryl substituent at the pyrazole 3-position (Scheme **1**) triggered an explosion of Tp-based metalloenzyme models, which has continued unabated for the past 30 years. The flexibility and robust nature of the $[HB(X)_3]^-$ framework has also encouraged the development of

Tp-variants in which the pyrazole donors are replaced by thioimidazoles,**4** *N*-heterocyclic carbenes,**5** triazoles,**6** or other heterocycles.**7** Fifty years after their discovery, scorpionates have a secure and ever-expanding presence in the synthetic (bio)inorganic toolbox.

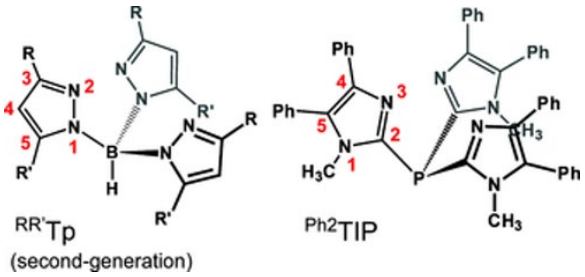

Scheme 1

Second-generation ^{R}Tp ligands are commonly used to mimic histidine-rich active sites that exhibit facial coordination at the metal ion(s); prominent examples include carbonic anhydrase,**8** copper-containing amine oxidase,**9** hemocyanin,**10** and copper nitrite reductases**11** (just to name a few). Scorpionates are also well-suited for biomimetic studies of mononuclear nonheme iron dioxygenases (MNIDs), which catalyze the incorporation of both atoms of O_2 into a wide variety of substrates.**12** The vast majority of MNIDs contain a high-spin Fe^{II} center bound by one Asp (or Glu) and two His residues in a facial orientation – the 2-His-1-carboxylate (2H1C) facial triad.**13** Numerous studies have employed the ^{R}Tp scaffold to replicate the monoanionic charge, facial arrangement, and ligand-field strength of the 2H1C triad.**14** Other chemists have prepared *N*,*N*,*O*-heteroscorpionates with one carboxylate and two nitrogen donors to more accurately reproduce the enzymatic ligand set.**15**

Given the prevalence of the 2H1C coordination motif among MNIDs, it was rather surprising when two crystal structures of mammalian cysteine dioxygenase (CDO), published in 2006, revealed a mononuclear iron site with a neutral 3-histidine (3His) facial triad instead.**16** Other members of the "3His family" were subsequently reported and structurally characterized, including β-diketone dioxygenase (Dke1),**17** salicylate 1,2-dioxygenase (SDO),**18** and gentisate 1,2-dioxygenase (GDO).**19** Of particular relevance to this manuscript is GDO, which catalyzes the oxid-ative cleavage of the C1–C2 bond within the hydroquinone ring of its substrate (Scheme **2**).**20** Interestingly, GDO is the only known example of a hydroquinone dioxygenase (HQDO) featuring the 3His triad;**21** all other HQDOs, including homogentisate dioxygenase, possess the canonical 2H1C triad.**22**

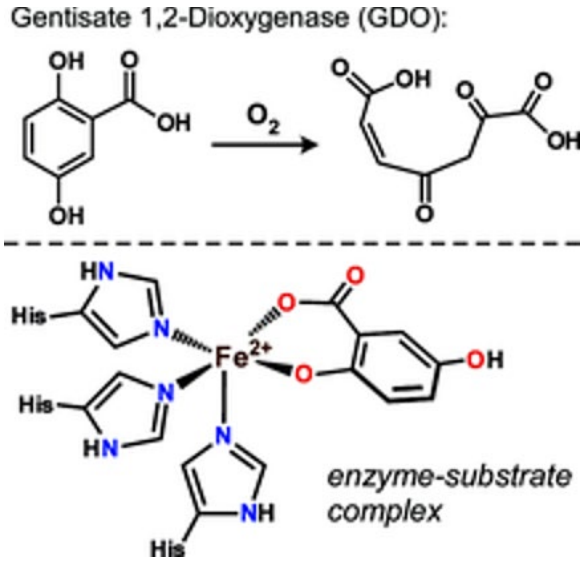

Scheme 2

The HQDO family is unique in containing both 2H1C and 3His enzymes, and the catalytic implications of this variation in first-sphere coordination environment are unclear at the present. Biomimetic studies involving both neutral and anionic scorpionates have the potential to elucidate the role of the facial triad in tuning the electronic structure of nonheme iron sites. In 2012, we reported a series of HQDO model complexes using the hydridotris(3,5-diphenylpyrazol-1-yl)borate (^{Ph2}Tp) supporting ligand to mimic the 2H1C triad found in most HQDOs.**23** Each complex featured a mono- or bidentate hydroquinonate (HQate) ligand attached to the $[Fe^{2+}(^{Ph2}Tp)]^{+}$ scaffold, thereby replicating the structure of substrate-bound HQDOs in which the deprotonated HQ coordinates directly to iron. The discovery of a 3His triad in the GDO active site has since prompted us to prepare HQDO models using a neutral, imidazole-based scorpionate ligand, specifically, tris(4,5-diphenyl-1-methylimidazol-2-yl)phosphine (^{Ph2}TIP; Scheme **1**). Tris(imidazolyl)phosphine ligands were initially developed in the 1980s to model the active sites of Zn and Cu enzymes.**24** Our previous spectroscopic studies of Dke1 models found that TIP ligands accurately reproduce the coordination environment and donor strength of the 3His triad, whereas the properties of Tp ligands align better with the 2H1C triad.**25** The ^{Ph2}Tp- and ^{Ph2}TIP-based complexes are therefore complimentary models of the two types of HQDO active sites.

This manuscript describes the synthesis and X-ray crystal structure of [Fe(^{Ph2}TIP)(BIHQ)]OTf {**1a**, where BIHQ is the monoanion of 2-(1-methyl-1*H*-benzimidazol-2-yl)hydroquinone; Scheme **3**}. The BIHQ ligand forms a six-membered chelate ring upon metal binding, which resembles the bidentate coordination of gentisate to iron in the GDO mechanism. The structural and electrochemical properties of **1a** are then compared to those previously reported for [Fe(^{Ph2}Tp)(BIHQ)] (**1b** in Scheme **3**; ^{Ph2}TIP-based complexes are labeled **Xa** and ^{Ph2}Tp-based complexes are labeled **Xb**). In addition, we have explored the ability of these complexes to perform proton- and electron-transfers via stepwise or concerted processes. For **1a** and **1b**, one-electron oxidation generates the corresponding Fe^{III}-HQate complexes **2a** and **2b**. Interestingly, both **2a** and **2b** undergo reversible deprotonation to yield metastable species (**3a** and **3b**, respectively) in which the Fe^{II} center is bound to a *p*-semiquinonate (*p*$SQ^{\bullet-}$) radical. The existence of this proton-induced valence tautomerization has been confirmed through extensive spectroscopic and computational studies. Complexes **3a** and **3b** serve as a models of

the elusive Fe^{II}-*p*$SQ^{\bullet-}$ intermediate proposed for the enzymatic mechanisms of HQDOs.**26** Moreover, the pairs of valence tautomers highlight the interplay of "noninnocent" behavior and protonation state for ligands associated with nonheme iron centers.

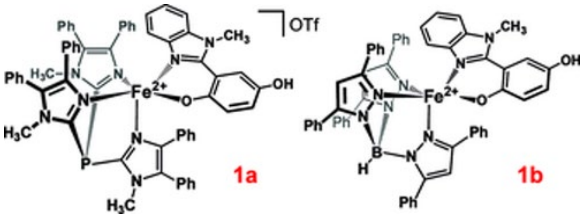

Scheme 3

II. Results and Discussion

1. Preparation, Solid-State Structures, and Electrochemical Properties

Complex **1a** was synthesized by the reaction of $[Fe(^{Ph2}TIP)(MeCN)_3](OTf)_2$**27** with an equimolar amount of Na(BIHQ) salt in THF. Yellow crystals, of sufficient quality for X-ray diffraction (XRD) analysis, were grown by vapor diffusion of diethyl ether into a concentrated 1,2-dichloroethane (DCE) solution. The asymmetric unit of the X-ray structure consists of the cationic monoiron complex, the triflate counteranion, and two Et_2O solvates. As shown in Figure **1** (a), the five-coordinate (5C) Fe^{II} center of **1a** is attached to a facially capping ^{Ph2}TIP ligand and bidentate BIHQ anion. The distorted coordination geometry is intermediate between square-pyramidal and trigonal-pyramidal. The two rings of the BIHQ chelate are rotated by 27° with respect to each other, largely to accommodate the π–π stacking interaction between the benzimidazole unit and a nearby 4-phenyl substituent of ^{Ph2}TIP. The distal –OH moiety of BIHQ forms a hydrogen bond with one of the Et_2O solvates.

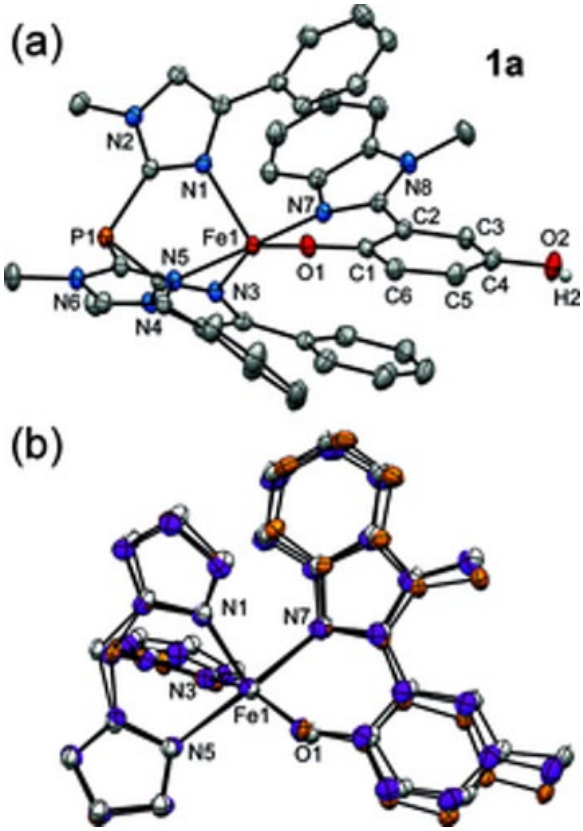

Figure 1 (a) Thermal ellipsoid plot (50 % probability) obtained from the X-ray crystal structure of **1a**. The phenyl rings at the 5-positions of the ^{Ph2}TIP ligand have been omitted for clarity, as well as non-coordinating solvent molecules and most hydrogen atoms. (b) Overlays of the crystallographically derived structures of **1a** (white), **1b** (orange), and **2b** (magenta). The phenyl and methyl substituents of the ^{Ph2}Tp and ^{Ph2}TIP ligands are not shown.

The Fe–N_{TIP} bond lengths of **1a** range from 2.11 Å for N3 to 2.22 Å for the pseudo-axial N5 donor (Table **1**). The anionic BIHQ ligand exhibits Fe1–O1 and Fe1–N7 distances of 1.91 and 2.15 Å, respectively, typical of phenolate**28** and benzimid-azole**29** donors in high-spin ferrous complexes. The observed magnetic moment of μ_{eff} = 4.93 μ_B at room temperature (r.t.) is also proof that **1a** possesses a high-spin (S = 2) Fe^{II} center.

Table 1. Selected bond lengths [Å] and bond angles [°] for complexes **1a**, **1b**, and **2b** as measured by X-ray crystallography

Bond lengths	**1a**	**1b a**	**2b**
Fe–N1	2.1681(12)	2.1218(14)	2.0409(17)
Fe–N3	2.1149(12)	2.1481(15)	2.0464(18)
Fe–N5	2.2214(12)	2.1470(15)	2.1138(17)
Fe–O1	1.9144(10)	1.9609(12)	1.8292(15)
Fe–N7	2.1503(13)	2.1393(15)	2.0693(17)
Fe–$N_{Tp/TIP}$ (ave)	2.168	2.139	2.067
Fe–L (ave)	2.114	2.103	2.020
O1–C1	1.321(2)	1.341(2)	1.337(2)
O2–C4	1.377(2)	1.370(2)	1.373(3)

C1–C2	1.423(2)	1.417(2)	1.412(3)
C1–C6	1.409(2)	1.405(2)	1.399(3)
C2–C3	1.410(2)	1.410(2)	1.403(3)
C3–C4	1.380(2)	1.379(2)	1.384(3)
C4–C5	1.393(2)	1.397(2)	1.390(3)
C5–C6	1.385(2)	1.383(2)	1.376(3)
C–C (ave)	1.400	1.399	1.394
C–C (dev) [b]	0.017	0.015	0.013
Bond angles			
O1–Fe–N1	117.31(5)	110.64(5)	115.58(7)
O1–Fe–N3	147.79(5)	153.34(5)	147.84(7)
O1–Fe–N5	98.33(4)	94.78(5)	94.80(7)
O1–Fe–N7	88.20(5)	88.90(5)	88.92(7)
N1–Fe–N3	94.87(5)	95.65(6)	96.52(7)
N1–Fe–N5	88.04(5)	92.11(5)	90.95(7)
N1–Fe–N7	89.69(5)	90.69(6)	91.19(7)
N3–Fe–N5	83.23(5)	79.38(6)	82.10(7)
N3–Fe–N7	90.82(5)	95.37(6)	92.54(7)
N5–Fe–N7	173.42(5)	174.27(6)	174.42(7)
τ-value [c]	0.43	0.35	0.44

[a] The structure of **1b** was originally reported in ref.22

[b] This number reflects the standard deviation of C–C bond lengths.

[c] See ref.29 for the definition of the τ-value.

Table **1** compares the metric parameters of ^{Ph2}TIP-based **1a** to those previously reported for ^{Ph2}Tp-based **1b**. The coordination geometries of the two complexes are quite similar, as evident in the overlay of solid-state structures shown in Figure **1** (b). The **1b** structure falls somewhat closer to the square-pyramidal limit than **1a**, as indicated by the respective τ-values**30** of 0.35 and 0.43 (Table **1**). The average Fe–N_{TIP} bond length in **1a** is about 0.03 Å longer than the average Fe–N_{Tp} bond length in **1b**, in line with our previous comparisons of Fe^{II} Tp/TIP pairs.**25**, **31**

The redox properties of **1a** were examined using electrochemical methods in CH_2Cl_2 solution with 0.1 m $[NBu_4]PF_6$ as the supporting electrolyte. All redox potentials are referenced to the ferrocene ($Fc^{+/0}$) couple. Two features are evident in the cyclic voltammogram (CV): a quasi-reversible couple at –190 mV (ΔE = 200 mV) and an irreversible oxidation at $E_{p,a}$ = 950 mV (Figure **2**). Based on our prior experience with **1b** and related complexes, the lower-potential event is assigned to the $Fe^{2+/3+}$ couple, while the high-potential peak is attributed to oxidation of the BIHQ ligand.**23**, **25**, **31** CV data obtained for **1b** is provided in Figure **2** for the sake of comparison. The $Fe^{2+/3+}$ potential of **1a** is shifted positively by 100 mV relative to **1b** due to the weaker donor strength of neutral ^{Ph2}TIP relative to anionic ^{Ph2}Tp.

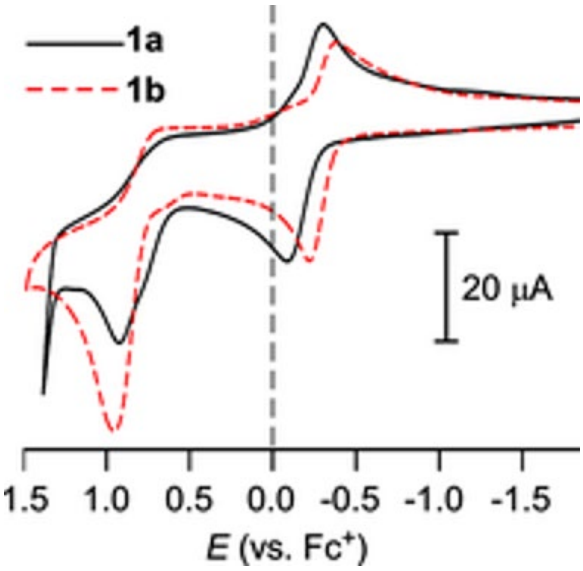

Figure 2 Cyclic voltammograms of **1a** and **1b** in CH_2Cl_2 (*c* = 2.0 mm) with 0.1 m $(NBu_4)PF_6$ as the supporting electrolyte.

On the basis of the CV data, we sought to isolate the ferric complexes **2a** and **2b** using chemical means of oxidation. To this end, treatment of the yellow Fe^{II} complexes with one equivalent of a ferrocenium (Fc^+) salt in CH_2Cl_2 gives rise to dark brown chromophores with intense absorption bands in the visible region (Figure **3**). The spectrum of **2a** exhibits a broad feature with λ_{max} = 630 nm (ε = 2600 m^{-1} cm^{-1}), while **2b** displays two intense, overlapping bands between 400 and 600 nm. These features likely arise from phenolate-to-Fe^{III} charge transfer (CT) transitions.**32** Indeed, both complexes exhibit EPR signals characteristic of rhombic, high-spin Fe^{III} centers; namely, an intense derivative-shaped feature at *g* = 4.3 and a much weaker peak at *g* = 9.4 (Figure **4** and S1).

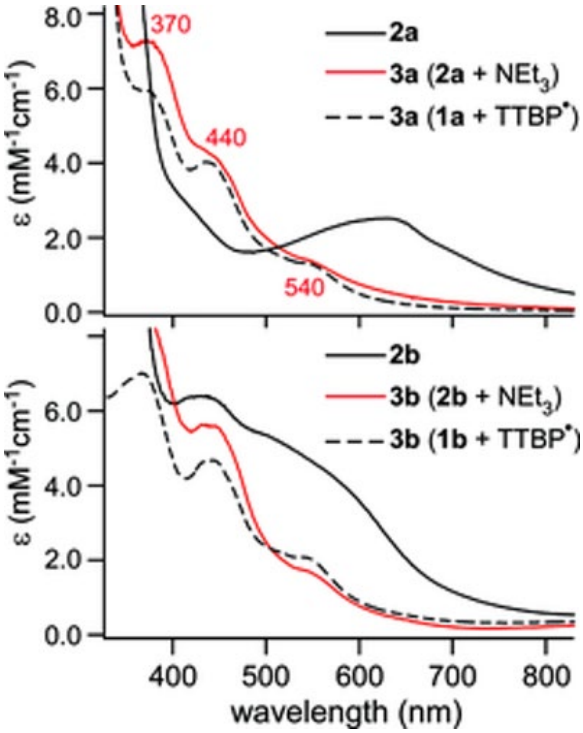

Figure 3 UV/Visible absorption spectra measured in CH_2Cl_2. The red spectra of **3a**/**3b** were obtained by treating solutions of **2a**/**2b** (black solid lines) with 5 equiv. of NEt_3 at –30 °C and r.t., respectively. The black spectra of **3a**/**3b** (dashed lines) were collected after treating solutions of **1a**/**1b** with one equiv. of the $TTBP^{\cdot}$ radical at room temp.

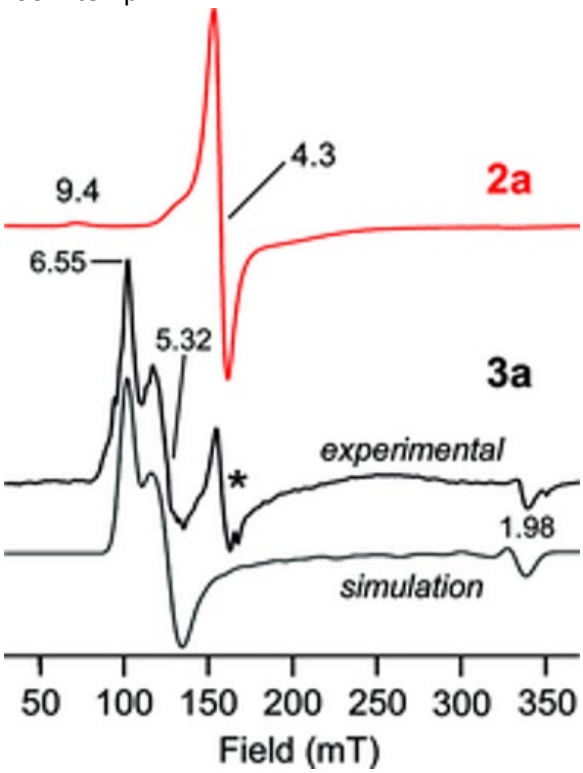

Figure 4 X-band EPR spectra of **2a** (red line) and **3a** (black line) in frozen CH_2Cl_2 solution ([Fe] = 1.4 mm) at 15 K. The intensity of the **2a** spectrum has been reduced by 50 %. The feature labeled with an asterisk (*) in the **3a** spectrum arises from residual **2a**. The simulated **3a** spectrum (grey line) was obtained with the following parameters: D = 0.63 cm^{-1}, E/D = 0.03, and g = 2.02, 2.0, 2.0.

Crystals of **2b** suitable for XRD studies were generated by oxidation with $[Fc]PF_6$, followed by diffusion of pentane into a concentrated DCE solution (to date, we have not been able to grow crystals of **2a** with any counteranion). Metric parameters derived from the resulting crystal structure are shown in Table **1**. Complex **2b** retains the five-coordinate geometry of its ferrous precursor, as illustrated by the high degree of overlap between the **1b** and **2b** structures depicted in Figure **1** (b). The presence of the distal –OH moiety of BIHQ is evident from the hydrogen bond it forms with the PF_6^- counteranion. Compared to **1b**, the average Fe–N_{Tp} and Fe–O1 bond lengths in **2b** are contracted by 0.07 and 0.13 Å, respectively, while the O–C and C–C distances of the BIHQ ligand are unchanged within experimental error (Table **1**). Therefore, the XRD data confirm that conversion of **1b** into **2b** involves an iron-centered oxidation, and there is no detectable amount of radical character on the BIHQ ligand. Although XRD data is lacking for **2a**, the spectroscopic results (vide supra) indicate that this complex also contains an Fe^{III} center bound to a HQate ligand.

2. Formation and Spectroscopic Features of 3a and 3b

Treatment of complexes **2a** and **2b** with 5–10 equiv. of triethylamine in CH_2Cl_2 immediately yields the golden-brown chromophores **3a** and **3b**, respectively (Figure **3**). The absorption spectra of the new species are nearly identical, with each displaying three bands of increasing intensity at 540, 440, and

370 nm. The reaction is reversible, as addition of excess acid (HBF_4) to solutions of **3a**/**3b** regenerates the **2a**/**2b** spectra with only 15 % reduction in intensity (Figure S2). Given the structure of the Fe^{III} complexes, it is reasonable to assume that the **2a**/**b** → **3a**/**b** conversion involves deprotonation of the distal –OH group of the BIHQ ligand. In support of this conclusion, **3a** and **3b** can also be prepared by treatment of the ferrous precursors (**1a** and **1b**) with 2,4,6-tri-*tert*-butylphenoxy radical ($TTBP^{\cdot}$) – a well-established H-atom transfer (HAT) agent (Figure **3**).**33** Thus, the three complexes in each series (**1a**/**1b**, **2a**/**2b**, **3a**/**3b**) can be interconverted by concerted or stepwise transfers of one electron and/or one proton, as indicated in Scheme **4**.

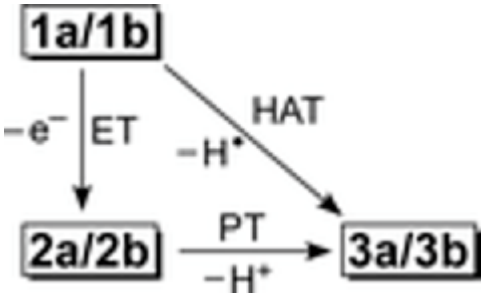

Scheme 4

Bases other than NEt_3 were used in an attempt to estimate the pK_a of **2a** and **2b**. For both complexes, addition of the weaker base 2,6-lutidine in CH_2Cl_2 failed to generate the corresponding **3a**/**3b** species. Similar results were observed for **2a** in MeCN solutions, where the pK_a-values of triethylammonium ($HNEt_3^+$) and 2,6-lutidinium (2,6-$LutH^+$) are known to be 18.6 and 14.0, respectively.**34** Bordwell and Mayer have proven that the bond dissociation free energy (BDFE) of an X–H bond is a function of both pK_a and redox potential ($E°$), according to the following equation: BDFE (X–H) = 1.37 pK_a + 23.06 $E°$ + $C_{G,solv}$, where $C_{G,solv}$ is a solvent-dependent constant equal to 54.9 kcal mol^{-1} in MeCN.**35** Using the experimental redox potential, and assuming a pK_a-value halfway between $HNEt_3^+$ and 2,6-$LutH^+$, provides a BDFE of 72.9 kcal mol^{-1} for **1a**. This bond energy is reasonable given that **1a** transfers a H-atom to $TTBP^{\cdot}$ (BDFE = 77.1 kcal mol^{-1}) but not to the $TEMPO^{\cdot}$ radical (BDFE = 66.5 kcal mol^{-1}; all values in MeCN).**35**

Unfortunately, it was not possible to grow crystals of **3a** or **3b** for XRD studies; therefore, electronic-structure insights were gathered using spectroscopic methods, in conjunction with the DFT calculations described in the next section. Two limiting descriptions are possible: **3a**/**3b** could consist of an Fe^{III} center bound to a closed-shell hydroquinonate dianion ($HQate^{2-}$), or an Fe^{II} center bound to a *p*-semiquinonate radical anion ($pSQ^{\cdot-}$). Significantly, the UV/Vis absorption spectra of **3a**/**3b** closely resemble those published for *para*- and *ortho*-semiquinone radicals in various contexts.**36** For example, our group recently prepared a ^{Ph2}Tp-based Fe^{II} complex that features a 1,4-naphthosemiquinone ligand. This complex displays a three-band pattern between 380 and 560 nm with intensities very similar to those observed for **3a**/**3b**.[**36**] Transient absorption studies of “free” *p*-semiquinones likewise report a series of π–π* transitions in the near-UV region.**37** Indeed, the close similarity of the **3a** and **3b** spectra suggests that the observed transitions are primarily ligand-based – a hypothesis supported by time-dependent DFT calculations (vide infra).

EPR samples of **3a** and **3b** were prepared via stepwise oxidation and deprotonation of **1a**/**1b**. Interestingly, it was observed that CH_2Cl_2 solutions of **3b** change color from golden-brown to green upon freezing, whereas **3a** maintains its brown color at all temperatures. Variable-temperature absorption studies found that the 440 and 540 nm bands of **3b** diminish as the temperature is lowered to –70 °C, while a new chromophore (labeled **4b**) appears with a broad band at λ_{max} = 825 nm. This thermochromic behavior is reversible, as **4b** converts back to **3b** when the temperature is returned to 25 °C (Figure S3). The EPR spectrum of **4b** measured at 15 K is featureless apart from a weak peak at g = 4.3 due to residual **2b** (Figure S1). While further studies are required, we postulate that **4b** arises from dimerization of **3b** at low temperatures, which would yield the EPR-silent species observed experimentally.

Thankfully, the absence of thermochromism for **3a** indicates that the structure of this complex is maintained upon freezing. Unlike **4b**, complex **3a** exhibits an intense EPR signal at 10 K with features at g = 6.55, 5.32, and 1.98, along with a small derivative at g = 4.3 from residual **2a** (Figure **4**). This spectrum is characteristic of an S = 5/2 paramagnet with an axial **D**-tensor; the data was nicely simulated with spin-Hamiltonian parameters of g = 2.02, 2.0, 2.0; D = 0.63 cm^{-1}, E/D = 0.03 (Figure **4**; where D and E are the axial and rhombic zero-field splitting parameters, respectively). Given the rhombic nature of the **2a** spectrum ($E/D \approx 0.33$) noted above, the EPR results make it clear that the **2a** → **3a** conversion causes a dramatic rearrangement of unpaired spin-density within the S = 5/2 manifold. The origin of this change has been elucidated with the aid of DFT calculations described in the next section.

3. Geometric and Electronic Structures of DFT-Optimized Models

Table **2** provides relevant metric parameters for energy-minimized structures of complexes **2b**, **3a**, and **3b** obtained via DFT geometry optimizations. Truncated versions of the complexes were employed in which the Ph rings at the 5-positions of the ^{Ph2}Tp and ^{Ph2}TIP ligands were removed. Unless otherwise noted, all calculations employed the hybrid B3LYP functional and assumed a S = 5/2 ground state. The accuracy of our computational approach was gauged by comparing the XRD and DFT structures of complex **2b**. While DFT slightly overestimates the Fe^{III}–N/O bond lengths (by 0.05 Å on average), it accurately reproduces the C–C and O–C bond lengths of the HQate ligand, with a root-mean-square deviation of only 0.01 Å (i.e., near the experimental 3σ error of the XRD measurement). We therefore felt confident in proceeding with calculations of **3a** and **3b**, for which structural data are lacking.

Table 2. DFT-calculated bond lengths [Å] for models of **2a**, **3a**, **3b**, and the BISQ radical

	2b	**3b**	**Δ a**	**3a**	**Free BISQb**
Bond distances					
Fe–N1	2.110	2.180	0.070	2.214	
Fe–N3	2.084	2.177	0.093	2.186	
Fe–N5	2.162	2.250	0.088	2.348	
Fe–O1	1.861	1.982	0.121	1.952	
Fe–N7	2.152	2.190	0.038	2.185	
Fe–L (av.)	2.074	2.156	0.082	2.177	
O1–C1	1.320	1.293	–0.027	1.303	1.327
O2–C4	1.360	1.256	–0.104	1.254	1.253

C1–C2	1.421	1.444	0.023	1.438	1.441
C1–C6	1.409	1.432	0.023	1.428	1.416
C2–C3	1.404	1.386	–0.018	1.386	1.383
C3–C4	1.388	1.442	0.054	1.441	1.444
C4–C5	1.401	1.448	0.047	1.448	1.447
C5–C6	1.409	1.361	–0.048	1.362	1.362
C–C (av.)	1.400	1.419	0.019	1.417	1.416
C–C (dev.)c	0.016	0.036		0.035	0.036
Mulliken spins					
Fe	4.14	3.81	–0.33	3.80	–
O,*N*-ligand	0.34	1.09	+0.75	1.13	1.04

[a] Difference between corresponding **2b** and **3b** bond lengths.
[b] Geometry-optimized model of the BISQ radical (H-atom removed from the 4-OH position).
[c] Standard deviation of the six C–C bond lengths within the BIHQ or BISQ ring.

The structural differences between **2b** and **3b**/**3a** are highlighted in Table **2**. The iron-ligand bonds in **3b** are longer than their counterparts in **2b** by an average of 0.082 Å; indeed, the computed Fe–L distances in **3a** and **3b** are more similar to those observed experimentally for the Fe^{II} complexes **1a**/**1b**.**38** The bidentate *O*,*N*-ligand derived from BIHQ also experiences sizeable changes. The closed-shell nature of the HQate donor in **2b** is evident in the uniformity of its six C–C bond lengths (standard deviation of 0.016 Å). In the **3a** and **3b** models, however, this deviation increases to 0.035 Å and the C–C bonds display the "four long/two short" pattern characteristic of semiquinones.**39** This quinoidal-type distortion is also apparent in the dramatic shortening of the O2–C4 bond from 1.360 Å in **2b** to ca. 1.255 Å in **3a**/**3b**. Significantly, the metric parameters of the bidentate *O*,*N*-ligand in **3a**/**3b** are very similar to those computed for the "free" 2-(1-methylbenzimidazol-2-yl)semiquinone radical ($BISQ^{\bullet}$; Table **2**). Collectively, the DFT results indicate that deprotonation of the distal –OH moiety triggers an electron transfer (ET) from BIHQ to the Fe center, giving rise to an Fe^{II}-BISQ configuration. This conclusion is further supported by the Mulliken spin populations of the Fe center (3.8 α spins) and BISQ ligand (1.1 α spins) in the **3a**/**3b** models (Table **2**).

DFT calculations of **3b** were used to generate the molecular orbital (MO) diagram shown in Figure **5**. The most critical orbitals for evaluating the electronic configuration of this complex are the frontier MOs in the spin-down (β) manifold. The highest-occupied β MO (203β) possesses 81 % Fe character with electron density primarily located in the Fe d_{yz} orbital, confirming the presence of a high-spin Fe^{II} ion. By contrast, the lowest-unoccupied β MO (204β) has 84 % ligand character localized in a π*-orbital on the $p SQ^{\bullet-}$ unit, clear evidence of a ligand-based radical. Ferromagnetic coupling between the Fe^{II} center (S = 2) and BISQ radical (S = 1/2) yields the axial S = 5/2 paramagnet observed in the EPR spectrum of **3a**.

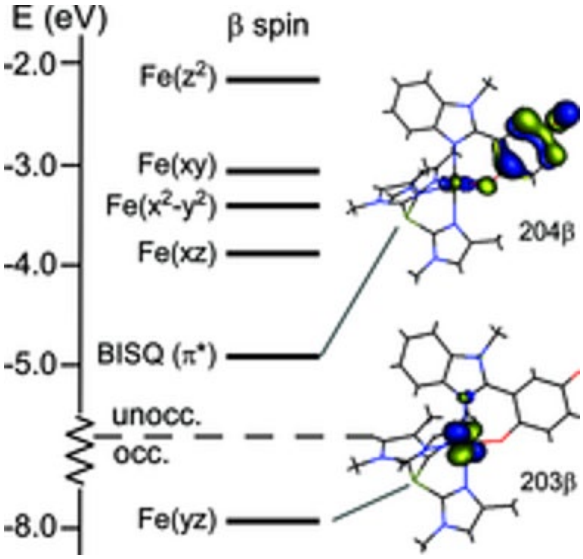

Figure 5 Energy-level diagram for the spin-down (β spin) MOs obtained from an unrestricted DFT calculation of **3a**. MOs are labeled according to their principal contributor. Surface contour plots for the highest-occupied and lowest-unoccupied orbitals are also shown.

The time-dependent DFT (TD-DFT) approach was employed to compute the absorption spectrum of **3a**. As shown in Figure **6**, the calculated spectrum adequately reproduces the energies and intensities of the experimental absorption features, suggesting that our DFT model of **3a** provides an accurate description of the complex's electronic structure. Analysis of the computed transitions indicate that the lowest-energy feature near 550 nm arises from an Fe^{II}→BISQ charge transfer (CT) transition, while the higher-energy peaks (350 nm < λ_{max} < 450 nm) are due to BISQ-based π→π* transitions. These findings are consistent with our prior studies of a monoiron(II) complex containing a 1,4-naphthosemiquinone ligand.[**36**]

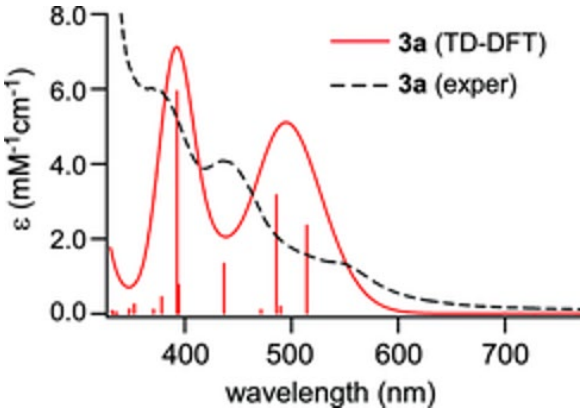

Figure 6 Experimental (black dashed line) and TD-DFT computed (solid red line) absorption spectra of **3a**. The experimental spectrum was obtained by treating **1a** with the $TTBP^{\cdot}$ radical in CH_2Cl_2. The red sticks mark the wavelengths and intensities of computed transitions.

To ensure that our computational results were not simply due to our chosen methodology, we also performed parallel calculations of **3a** and **3b** with the *non-hybrid* Becke–Perdew 86 functional (BP). As shown in Table S1, the ligand metric parameters of the BP optimized structures are nearly identical to those obtained with B3LYP (rms deviation of 0.009 Å), although the Fe–N/O distances computed by BP

are shorter by ca. 0.04 Å on average. Importantly, the bonding descriptions and spin-density distributions provided by the BP calculations are indicative of an Fe^{II}-BISQ electronic configuration for **3a**/**3b**, in agreement with the B3LYP results.

4. Resonance Raman Spectroscopic Studies

The electronic structures of complexes **3a** and **3b** were further examined with resonance Raman (rR) spectroscopy – a well-established method for the characterization of semiquinone radicals.**40** The experiments employed 457.9 nm laser excitation, in resonance with the ligand-based π–π* transition observed near 440 nm. Spectra of **3b** and its **2b** precursor were measured at 273 K due to the thermochromic nature of the former complex (vide supra), whereas the **3a** spectrum was collected at 77 K on a frozen sample. Figure **7** highlights the 1200–1700 cm^{-1} region where peaks due to aromatic C–C and O–C stretching modes are typically found. The **3a** and **3b** spectra exhibit an intense feature near 1527 cm^{-1} that is not apparent in the **2a** spectrum, and it arises regardless of the route of preparation (concerted H-atom transfer or sequential oxidation/deprotonation). A series of peaks is also evident between 1400 and 1500 cm^{-1}, especially in the low-temperature **3a** spectrum.

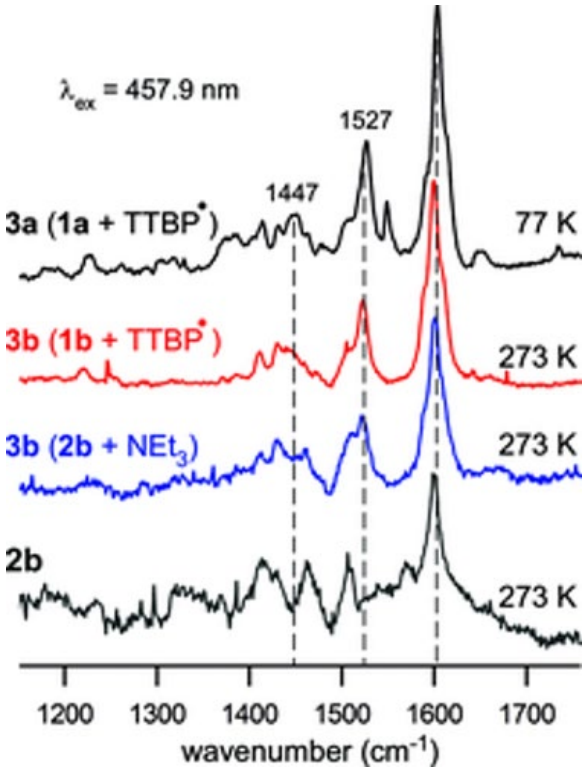

Figure 7 Resonance Raman spectra obtained with 457.9 nm excitation (40 mW at sample) of **2b**, **3a**, and **3b** in CD_2Cl_2 solutions. The **3a** sample was prepared by treatment of the **1a** precursor with $TTBP^{\cdot}$. The rR spectrum of **3a** (black line) was collected at 77 K. Samples of **3b** were prepared via two routes: treatment of **1b** with $TTBP^{\cdot}$ (red spectrum) or addition of 5 equiv. of NEt_3 to **2b** (blue spectrum). rR spectra of **3b** and **2b** (gray line) were measured at 273 K (ice/water bath).

To aid in assignment of the observed rR peaks, DFT frequency calculations were performed for the BIHQ ligand in three oxidation states: the hydroquinonate anion (BIHQate; deprotonated at 4-OH position), semiquinone radical (BISQ; H-atom removed from 4-OH position), and benzoquinone (BIBQ). We focused specifically on the predicted frequency of the distal O–C stretching mode [ν(O2–C4)], since

studies of *ortho*-dioxolene compounds have demonstrated that ν(O–C) modes give rise to intense rR peaks that are diagnostic of ligand oxidation state.**40** The computed ν(O2–C4)-based mode appears at 1414 and 1681 cm^{-1} for BIHQate and BIBQ, respectively, following the expected increase in frequency as the ligand becomes more oxidized. The BISQ calculation predicts two modes with significant ν(O2–C4) character at intermediate frequencies of 1449 and 1521 cm^{-1}. The 1449 cm^{-1} vibration couples the ν(O2–C4) stretch with the breathing motion of the *p*SQ ring, while the 1521 cm^{-1} vibration couples the ν(O2–C4) stretch to nearby bending motions. Significantly, these calculated ν(O2–C4) frequencies are consistent with previous studies of *p*SQ radicals**41** and remarkably close to the experimentally observed peaks at 1527 and ca. 1450 cm^{-1} in the **3a**/**3b** spectra (Figure **7**). Thus, the rR data provide further evidence that complexes **3a** and **3b** possess a BISQ ligand.

III. Summary and Conclusions

This manuscript has described the preparation and X-ray structural characterization of complex **1a** (Scheme **3**) – the first synthetic model of the nonheme iron enzyme GDO. The mononuclear Fe^{II} center in the GDO active site is coordinated by a 3His facial triad (Scheme **2**), in contrast to the 2H1C triad found in all other HQDOs.**19** Complex **1a** features a neutral ^{Ph2}TIP scorpionate ligand to mimic the enzymatic 3His triad, while the bidentate BIHQ ligand models the coordination of gentisate to the Fe^{II} ion. The structural and electrochemical properties of **1a** were compared to those previously reported for the analogous complex **1b**, which contains a monoanionic ^{Ph2}Tp scorpionate ligand (Scheme **3**) that better resembles the 2H1C triad. Overall, the differences between **1a** and **1b** are modest: the Fe–N_{TIP} bonds are longer than the Fe–N_{Tp} distances by an average of 0.03 Å (Table **1**), and the $Fe^{3+/2+}$ redox potential of **1a** is shifted positively by ca. 100 mV relative to **1b** (Figure **2**). Future efforts will examine the comparative O_2 reactivities of **1a** and **1b** to ascertain the functional significance of the 3His/2H1C variation for HQDO catalysis. The present work further emphasizes the impressive utility of the scorpionate framework – first reported 50 years ago by Trofimenko – in biomimetic studies of nonheme iron enzymes.

Spectroscopic and crystallographic methods confirmed that one-electron oxidation of **1a** and **1b** yields the Fe^{III}-HQate complexes **2a** and **2b**. Treatment of the Fe^{III} complexes with excess NEt_3 gives rise to the brown chromophores **3a** and **3b**, which can also be generated by treatment of **1a**/**1b** with the H-atom abstracting agent, $TTBP^{\cdot}$ (Scheme **4**). Extensive spectroscopic (UV/Vis, EPR, rR) and computational (DFT) studies provided overwhelming evidence that **3a** and **3b** feature a high-spin Fe^{II} center ferromagnetically coupled to a $pSQ^{\cdot-}$ ligand (BISQ). Thus, the conversion of **2a**/**2b** → **3a**/**3b** involves both deprotonation of the distal hydroxyl group and intramolecular ligand-to-metal ET, as illustrated in Scheme **5** (a). The ET occurs because loss of the distal proton destabilizes of the frontier MOs of the HQate ligand relative to those of the iron center; indeed, it has been shown that deprotonation of free *p*-hydroquinonate lowers its redox potential by more than 0.9 V in DMSO.**35**, **42** Keramidas and co-workers have similarly demonstrated that tetranuclear vanadium(V) complexes with bridging HQate ligands undergo deprotonation to give the corresponding V^{IV}-SQate species.**43** Thus, there is literature precedent for the type of reversible, proton-induced valence tautomerization described here.

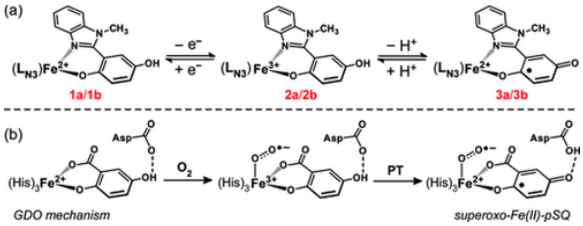

Scheme 5

Noninnocent (i.e., redox-active) ligands have garnered increasing attention due to their ability to function as electron reservoirs in the cycles of (bio)inorganic catalysts, thereby permitting multi-electron transformations.**44** By comparison, less attention has been paid to ligands, such as HQates, that are capable of donating (or accepting) both electrons *and protons*. The advantage of this type of noninnocent ligand is its potential to participate in proton-coupled electron transfers (PCETs), which play a critical role in numerous biological and synthetic processes.**35**, **45** The interconversions of **2a**/**3a** and **2b**/**3b** highlight the ability of protonation state to modulate the noninnocent nature of ligands such as BIHQ.

Significantly, this series of complexes (**1a**/**1b**, **2a**/**2b**, **3a**/**3b**) replicates key aspects of the proposed GDO mechanism, as shown in Scheme **5**. The active site of GDO contains a conserved second-sphere Asp residue that forms a hydrogen bond to the distal –OH group of the coordinated gentisate substrate.**19** It has been proposed that this second-sphere carboxylate moiety deprotonates gentisate during (or immediately after) O_2 binding to the Fe center, thereby giving rise to a superoxo-Fe^{II}-*p*$SQ^{\bullet-}$ intermediate, see Scheme **5** (b).**19**, **26** While this intermediate has not been observed experimentally, the synthetic results described here suggest that formation of an Fe^{II}-*p*$SQ^{\bullet-}$ intermediate via transfer of $1e^-$ and $1H^+$ is a viable option for the GDO catalytic cycle. Of course, the complexes **2a**/**2b** and **3a**/**3b** lack the superoxide ligand of the biological intermediates; therefore, efforts to generate iron-(semi)quinonate species via direct reaction of **1a**/**1b** with O_2 are currently underway.

Experimental Section

Materials and Physical Methods: Unless otherwise noted, all reagents and solvents were purchased from commercial sources and used as received. Solvents CH_2Cl_2 and MeCN were purified and dried using a Vacuum Atmospheres solvent purification system. The synthesis and handling of air-sensitive materials were performed under inert atmosphere using a Vacuum Atmospheres Omni-Lab glovebox. The compounds ferrocenium hexaflurorphosphate ([Fc]PF_6),**46** 2,4,6-tri-*tert*-butylphenoxyl radical (TTBP$^{\bullet}$),**33** ^{Ph2}TIP**27** and 2-(1-methylbenzimidazol-2-yl)hydroquinone**23** were prepared according to published procedures. The syntheses and X-ray crystal structures of complexes [Fe(^{Ph2}TIP)$(MeCN)_3$]$(OTf)_2$ and **1b** were reported previously.**23**, **27** Elemental analyses were performed at Midwest Microlab, LLC in Indianapolis, IN.

UV/Vis absorption spectra were collected with an Agilent 8453 diode array spectrometer equipped with a cryostat from Unisoku Scientific Instruments (Osaka, Japan) for experiments at reduced temperatures. Infrared (IR) spectra were measured with a Thermo Scientific Nicolet iS5 FTIR spectrometer equipped with the iD3 attenuated total reflectance accessory for solid-state samples.

EPR experiments were performed using a Bruker EleXsys E650 instrument equipped with an ER4415DM cavity, an Oxford Instruments ITC503 temperature controller, and an ESR-900 He flow cryostat. The program *EasySpin4* was used to simulate the experimental spectra.**47** Resonance Raman (rR) spectra were measured with 457.9 nm excitation from a Coherent I-305 Ar^+ laser using ca. 40 mW of power at the sample. The scattered light was collected using a 135° backscattering arrangement, dispersed by an Acton Research triple monochromator and detected with a Princeton Instruments Spec X 100BR CCD camera. The samples were held in a dewar cooled with either water/ice (273 K) or liquid nitrogen (77 K).

Electrochemical measurements were performed with an epsilon EC potentiostat (iBAS) under nitrogen atmosphere at a scan rate of 100 mV/s with 0.1 m $(NBu_4)PF_6$ as the electrolyte. A three-electrode cell containing a Ag/AgCl reference electrode, a platinum auxiliary electrode, and a glassy carbon working electrode was employed for cyclic and square-wave voltammetric measurements. Under these conditions, the ferrocene/ferrocenium ($Fc^{+/0}$) couple has an $E_{1/2}$ value of +0.52 V in CH_2Cl_2.

X-ray diffraction (XRD) data were collected with an Oxford Diffraction SuperNova kappa-diffractometer (Agilent Technologies) equipped with dual microfocus Cu/Mo X-ray sources, X-ray mirror optics, Atlas CCD detector, and low-temperature Cryojet device. The data were processed with CrysAlis Pro program package (Agilent Technologies, 2011), followed by an empirical multi-scan correction using SCALE3 ABSPACK routine. Structures were solved using SHELXS program and refined with SHELXL program**48** within Olex2 crystallographic package.**49** X-ray crystallographic parameters are provided in Table **3** and experimental details are available in the CIFs.

Table 3. Summary of X-ray crystallographic data collection and structure refinement

	1a·2Et$_2$Oa	**2b·C$_2$H$_4$Cl$_2$**
Empirical formula	$C_{71}H_{70}F_3FeN_8O_7PS$	$C_{61}H_{49}BCl_2F_6FeN_8O_2P$
Formula weight	1323.26	1208.61
Crystal system	monoclinic	triclinic
Space group	$P2_1/c$	$P\,1$
a [Å]	21.2966(19)	12.8542(5)
b [Å]	20.2553(16)	14.8267(4)
c [Å]	15.4880(15)	16.1415(5)
α [deg]	90	75.336(6)
β [deg]	101.9938(8)	68.675(3)
γ [deg]	90	88.313(3)
V [Å^3]	6535.20(10)	2765.67(15)
Z	4	2
$\varrho_{calcd.}$ [g/cm^3]	1.348	1.451
λ [Å]	1.5418	1.5418
μ [mm^{-1}]	3.042	3.970
ϑ range [deg]	6 to 149	6 to 149
Reflections collected	63087	52535
Independent reflections	13122 [R_{int} = 0.0320]	11084 [R_{int} = 0.0418]
Data/restraints/parameters	13122/0/868	11084/0/777
GOF (on F^2)	1.021	1.078

$R1/wR2$ [$I > 2\sigma(I)$]	0.0348/0.0907	0.0460/0.1234
$Ra/wR2$ (all data)	0.0378/0.0932	0.0495/0.1271

[a] One of the Et_2O solvates is partially (11 %) occupied by 1,2-dichloroethane solvent.

CCDC 1436476 (for **1a**), and 1436477 (for **2b**) contain the supplementary crystallographic data for this paper. These data can be obtained free of charge from **The Cambridge Crystallographic Data Centre**.

[Fe(^{Ph2}TIP)(BIHQ)]OTf (1a): Under an inert atmosphere, 2-(1-methyl-1*H*-benzimidazol-2-yl)hydroquinone (33 mg, 0.14 mmol) was deprotonated by stirring with one equivalent of NaOMe in THF. After 30 min, a solution of [Fe(^{Ph2}TIP)(MeCN)$_3$](OTf)$_2$ (165 mg, 0.14 mmol) in THF was added to the reaction vial. The mixture was stirred overnight, and the solvent was then removed under vacuum. The crude product was taken up in 1,2-dichloroethane and filtered through Celite. Vapor diffusion of Et_2O into this solution provided yellow crystals suitable for X-ray diffraction (113 mg, 71 %). $C_{63}H_{50}F_3FeN_8O_5PS$ (MW = 1175.02 g mol^{-1}): calcd. C 64.40, H 4.29, N 9.54; found C 63.80, H 4.82, N 9.04. UV/Vis (CH_2Cl_2): λ_{max} (ε, m^{-1} cm^{-1}) = 378 (7800), 440 (2200) nm. FTIR (solid): $\tilde{\nu}$ = 3590 [ν(O–H)], 3047, 2985, 2871, 1604, 1578, 1504, 1488, 1461, 1444, 1386, 1325, 1253, 1155, 1074, 1031, 949, 833, 638 cm^{-1}.

[Fe(^{Ph2}Tp)(BIHQ)]PF$_6$ (2b): Complex **1b** (149 mg, 0.15 mmol) was treated with one equivalent of [Fc]PF$_6$ (50 mg, 0.15 mmol) in MeCN (10 mL) for 30 min. The resulting dark brown solution was filtered through Celite to eliminate any unreacted precursor complex, and the solvent was removed under vacuum. The resulting brown solid was washed twice with pentane (3 mL each time) to extract the ferrocene byproduct. The crude product was then taken up in 1,2-dichloroethane (4 mL), and vapor diffusion of pentane into this solution yielded dark brown needles suitable for X-ray crystallography (145 mg, 87 %). $C_{59}H_{45}BF_6FeN_8O_2P$ (MW = 1109.68 g mol^{-1}): calcd. C 63.86, H 4.09, N 10.10; found C 63.49, H 4.25, N 10.05. UV/Vis (CH_2Cl_2): λ_{max} (ε, m^{-1} cm^{-1}) = 339 (12800), 441 (6250), 506 (5800) nm. FTIR (solid): 3529 [ν(O–H)], 3057, 2987, 2626 [ν(B–H)], 1545, 1479, 1425, 1354, 1255, 1165, 1067, 1013, 848, 781, 559 cm^{-1}.

DFT Computations: DFT calculations were performed using the ORCA 3.0 software package developed by Dr. F. Neese (MPI for Chemical Energy Conversion).**50** Geometry optimizations employed either (i) Becke's three-parameter hybrid functional for exchange along with the Lee–Yang–Parr correlation functional (B3LYP),**51** or (ii) the Becke–Perdew (BP86) functional.**52** The coordinates of the geometry-optimized models are provided in the Supporting Information (Tables S2–S9). All calculations used Ahlrichs' valence triple-ζ basis set (TZV) and TZV/J auxiliary basis set, in conjunction with polarization functions on all atoms.**53** In the geometry optimized models, the ^{Ph2}TIP and ^{Ph2}Tp ligands were modified by replacing the Ph-groups at the 5-positions of the imidazolyl and pyrazolyl rings, respectively, with H-atoms. Time-dependent DFT (TD-DFT) calculations of **3a** used a truncated version of the optimized model with Me groups (instead of Ph groups) at the 4-positions of the imidazolyl rings. TD-DFT calculations**54** provided absorption energies and intensities for 60 excited states with the Tamm–Dancoff approximation.**55** Vibrational frequency calculations were performed on the BIHQ ligand in various oxidation states; calculation of the harmonic force fields proved that the optimized structure is a local minima on the potential energy surface. Isosurface plots of molecular orbitals and electron-density difference maps (EDDMs) were prepared with Laaksonen's gOpenMol program.**56**

Supporting Information (see footnote on the first page of this article): DFT-calculated bond lengths for **3a** and **3b** using the BP functional (Table S1), Cartesian coordinates for all geometry-optimized structures (Tables S2–S9), and Figures S1–S3.

Acknowledgements

The authors are grateful to Dr. Thomas Brunold (University of Wisconsin - Madison) for access to EPR and rR instrumentation. This research received financial support from the U.S. National Science Foundation (NSF) (CHE-1056845). A. E. B. was the beneficiary of an Eisch Research Fellowship.

References

1 a) S. Trofimenko, in: Scorpionates: the coordination chemistry of polypyrazolylborate ligands, Imperial College Press, London, UK, 1999; b) C. Pettinari, in: Scorpionates II: chelating borate ligands, Imperial College Press, London, UK, 2008.

2 a) W. H. Armstrong and S. J. Lippard, J. Am. Chem. Soc., 1983, **105**, 4837– 4838; b) W. H. Armstrong and S. J. Lippard, J. Am. Chem. Soc., 1984, **106**, 4632– 4633.

3 a) S. Trofimenko, J. C. Calabrese and J. C. Thompson, Inorg. Chem., 1987, **26**, 1507– 1514; b) J. C. Calabrese, S. Trofimenko and J. S. Thompson, J. Chem. Soc., Chem. Commun., 1986, 1122– 1123.

4 M. Garner, J. Reglinski, I. Cassidy, M. D. Spicer and A. R. Kennedy, Chem. Commun., 1996, 1975– 1976.

5 a) U. Kernbach, M. Ramm, P. Luger and W. P. Fehlhammer, Angew. Chem. Int. Ed. Engl., 1996, **35**, 310– 312; Angew. Chem., 1996, **108**, 333; b) I. Nieto, F. Cervantes-Lee and J. M. Smith, Chem. Commun., 2005, 3811– 3813.

6 a) C. Janiak and H. Hemling, J. Chem. Soc., Dalton Trans., 1994, 2947– 2952; b) C. Janiak, J. Chem. Soc., Chem. Commun., 1994, 545– 547; c) K. B. Shiu, J. Y. Lee, Y. Wang and M. C. Cheng, Inorg. Chem., 1993, **32**, 3565– 3567; d) Z. Xiao, M. A. Bruck, C. Doyle, J. H. Enemark, C. Grittini, R. W. Gable, A. G. Wedd and C. G. Young, Inorg. Chem., 1995, **34**, 5950– 5962; e) B. C. Hughes, Z. Lu and D. M. Jenkins, Chem. Commun., 2014, **50**, 5273– 5275.

7 a) G. G. Lobbia, M. Pellei, C. Pettinari, C. Santini, N. Somers and A. H. White, Inorg. Chim. Acta, 2002, **333**, 100– 108; b) C. J. Snyder, P. D. Martin, M. J. Heeg and C. H. Winter, Chem. Eur. J., 2013, **19**, 3306– 3310.

8 a) G. Parkin, Chem. Rev., 2004, **104**, 699– 767; b) A. Looney and G. Parkin, Inorg. Chem., 1994, **33**, 1234– 1237; c) A. Looney, R. Han, K. McNeill and G. Parkin, J. Am. Chem. Soc., 1993, **115**, 4690– 4697; d) R. Han, A. Looney, K. McNeill, G. Parkin, A. L. Rheingold and B. S. Haggerty, J. Inorg. Biochem., 1993, **49**, 105– 121; e) A. Looney, G. Parkin, R. Alsfasser, M. Ruf and H. Vahrenkamp, Angew. Chem. Int. Ed., 1992, **31**, 92– 93; Angew. Chem., 1992, **104**, 57– 58; f) R. Alsfasser, S. Trofimenko, A. Looney, G. Parkin and H. Vahrenkamp, Inorg. Chem., 1991, **30**, 4098– 4100.

9 a) C. L. Foster, X. Liu, C. A. Kilner, M. Thornton-Pett and M. A. Halcrow, J. Chem. Soc., Dalton Trans., 2000, 4563– 4568; b) M. Gennari and L. Marchio, Curr. Bioact. Compd., 2009, **5**, 244– 263.

10 N. Kitajima, K. Fujisawa, C. Fujimoto, Y. Morooka, S. Hashimoto, T. Kitagawa, K. Toriumi, K. Tatsumi and A. Nakamura, J. Am. Chem. Soc., 1992, **114**, 1277– 1291.

11 A. C. Merkle and N. Lehnert, Dalton Trans., 2012, **41**, 3355– 3368.

12 a) E. I. Solomon, T. C. Brunold, M. I. Davis, J. N. Kemsley, S. K. Lee, N. Lehnert, F. Neese, A. J. Skulan, Y. S. Yang and J. Zhou, Chem. Rev., 2000, **100**, 235– 349; b) M. Costas, M. P. Mehn, M. P. Jensen and L. Que, Chem. Rev., 2004, **104**, 939– 986.
13 K. D. Koehntop, J. P. Emerson and L. Que, J. Biol. Inorg. Chem., 2005, **10**, 87– 93.
14 a) P. C. A. Bruijnincx, G. van Koten and R. J. M. K. Gebbink, Chem. Soc. Rev., 2008, **37**, 2716– 2744; b) N. Burzlaff, Angew. Chem. Int. Ed., 2009, **48**, 5580– 5582; Angew. Chem., 2009, **121**, 5688.
15 a) A. Beck, B. Weibert and N. Burzlaff, Eur. J. Inorg. Chem.., 2001, 521– 527; b) A. Beck, A. Barth, E. Hubner and N. Burzlaff, Inorg. Chem., 2003, **42**, 7182– 7188; c) P. C. A. Bruijnincx, M. Lutz, A. L. Spek, E. E. v. Faassen, B. M. Weckhuysen, G. v. Koten and R. J. M. K. Gebbink, Eur. J. Inorg. Chem.., 2005, 779– 787; d) P. C. A. Bruijnincx, I. L. C. Buurmans, S. Gosiewska, M. A. H. Moelands, M. Lutz, A. L. Spek, G. v. Koten and R. J. M. K. Gebbink, Chem. Eur. J., 2008, **14**, 1228– 1237; e) L. Peters, E. Huebner and N. Burzlaff, J. Organomet. Chem., 2005, **690**, 2009– 2016; f) P. C. A. Bruijnincx, M. Lutz, A. L. Spek, W. R. Hagen, B. M. Weckhuysen, G. van Koten and R. J. M. K. Gebbink, J. Am. Chem. Soc., 2007, **129**, 2275– 2286.
16 a) J. G. McCoy, L. J. Bailey, E. Bitto, C. A. Bingman, D. J. Aceti, B. G. Fox and G. N. PhillipsJr, Proc. Natl. Acad. Sci. USA, 2006, **103**, 3084– 3089; b) C. R. Simmons, Q. Liu, Q. Q. Huang, Q. Hao, T. P. Begley, P. A. Karplus and M. H. Stipanuk, J. Biol. Chem., 2006, **281**, 18723– 18733.
17 a) G. D. Straganz, A. R. Diebold, S. Egger, B. Nidetzky and E. I. Solomon, Biochemistry, 2010, **49**, 996– 1004; b) A. R. Diebold, M. L. Neidig, G. R. Moran, G. D. Straganz and E. I. Solomon, Biochemistry, 2010, **49**, 6945– 6952.
18 I. Matera, M. Ferraroni, S. Buerger, A. Scozzafava, A. Stolz and F. Briganti, J. Mol. Biol., 2008, **380**, 856– 868.
19 a) J. Chen, W. Li, M. Wang, G. Zhu, D. Liu, F. Sun, N. Hao, X. Li, Z. Rao and X. C. Zhang, Protein Sci., 2008, **17**, 1362– 1373; b) M. A. Adams, V. K. Singh, B. O. Keller and Z. Jia, Mol. Microbiol., 2006, **61**, 1469– 1484.
20 a) M. R. Harpel and J. D. Lipscomb, J. Biol. Chem., 1990, **265**, 6301– 6311; b) M. R. Harpel and J. D. Lipscomb, J. Biol. Chem., 1990, **265**, 22187– 22196.
21 D. Buongiorno and G. D. Straganz, Coord. Chem. Rev., 2013, **257**, 541– 563.
22 G. P. Titus, H. A. Mueller, J. Burgner, S. R. de Cordoba, M. A. Penalva and D. E. Timm, Nat. Struct. Biol., 2000, **7**, 542– 546.
23 A. E. Baum, H. Park, D. N. Wang, S. V. Lindeman and A. T. Fiedler, Dalton Trans., 2012, **41**, 12244– 12253.
24 a) R. S. Brown and J. Huguet, Can. J. Chem., 1980, **58**, 889– 901; b) R. Breslow, J. T. Hunt, R. Smiley and T. Tarnowski, J. Am. Chem. Soc., 1983, **105**, 5337– 5342; c) H. Slebockatilk, J. L. Cocho, Z. Frakman and R. S. Brown, J. Am. Chem. Soc., 1984, **106**, 2421– 2431; d) W. E. Allen and T. N. Sorrell, Inorg. Chem., 1997, **36**, 1732– 1734; e) C. Kimblin, W. E. Allen and G. Parkin, J. Chem. Soc., Chem. Commun., 1995, 1813– 1815; f) W. E. Lynch, D. M. Kurtz, S. K. Wang and R. A. Scott, J. Am. Chem. Soc., 1994, **116**, 11030– 11038; g) P. C. Kunz, G. J. Reiss, W. Frank and W. Klaui, Eur. J. Inorg. Chem.., 2003, 3945– 3951; h) P. C. Kunz and W. Klaeui, Collect. Czech. Chem. Commun., 2007, **72**, 492– 502.
25 H. Park, J. S. Baus, S. V. Lindeman and A. T. Fiedler, Inorg. Chem., 2011, **50**, 11978– 11989.
26 a) T. E. Machonkin and A. E. Doerner, Biochemistry, 2011, **50**, 8899– 8913; b) T. Borowski, V. Georgiev and P. E. M. Siegbahn, J. Am. Chem. Soc., 2005, **127**, 17303– 17314; c) S. Liu, T. Su, C. Zhang, W.-M. Zhang, D. Zhu, J. Su, T. Wei, K. Wang, Y. Huang, L. Guo, S. Xu, N.-Y. Zhou and L. Gu, J. Biol. Chem., 2015, **290**, 24547– 24560.
27 M. M. Bittner, J. S. Baus, S. V. Lindeman and A. T. Fiedler, Eur. J. Inorg. Chem.., 2012, 1848– 1856.

28 a) S. S. Rocks, W. W. Brennessel, T. E. Machonkin and P. L. Holland, Inorg. Chem., 2010, **49**, 10914– 10929; b) T. J. Boyle, L. A. M. Ottley, C. A. Apblett, C. A. Stewart, S. M. Hoppe, K. L. Hawthorne and M. A. Rodriguez, Inorg. Chem., 2011, **50**, 6174– 6182; c) A. V. Wiznycia, J. Desper and C. J. Levy, Can. J. Chem., 2009, **87**, 224– 231.
29 a) C.-C. Tsou, W.-L. Yang and W.-F. Liaw, J. Am. Chem. Soc., 2013, **135**, 18758– 18761; b) W.-H. Sun, P. Hao, S. Zhang, Q. Shi, W. Zuo, X. Tang and X. Lu, Organometallics, 2007, **26**, 2720– 2734; c) D. Gong, X. Jia, B. Wang, X. Zhang and L. Jiang, J. Organomet. Chem., 2012, **702**, 10– 18.
30 A. W. Addison, T. N. Rao, J. Reedijk, J. Vanrijn and G. C. Verschoor, J. Chem. Soc., Dalton Trans., 1984, 1349– 1356.
31 M. M. Bittner, D. Kraus, S. V. Lindeman, C. V. Popescu and A. T. Fiedler, Chem. Eur. J., 2013, **19**, 9686– 9698.
32 a) M. Ito, H. Amagai, H. Fukui, N. Kitajima and Y. Moro-oka, Bull. Chem. Soc. Jpn., 1996, **69**, 1937– 1945; b) J. W. Pyrz, A. L. Roe, L. J. Stern and L. QueJr, J. Am. Chem. Soc., 1985, **107**, 614– 620.
33 V. W. Manner, T. F. Markle, J. H. Freudenthal, J. P. Roth and J. M. Mayer, Chem. Commun., 2008, 256– 258.
34 K. Izutsu, in: Acid-Base Dissociation Constants in Dipolar Aprotic Solvents, vol. 35, Blackwell Scientific Publications, Oxford, UK, 1990.
35 J. J. Warren, T. A. Tronic and J. M. Mayer, Chem. Rev., 2010, **110**, 6961– 7001.
36 a) P. Wang, G. P. A. Yap and C. G. Riordan, Chem. Commun., 2014, **50**, 5871– 5873; b) A. E. Baum, H. Park, S. V. Lindeman and A. T. Fiedler, Inorg. Chem., 2014, **53**, 12240– 12242.
37 a) I. Amada, M. Yamaji, M. Sase and H. Shizuka, J. Chem. Soc. Faraday Trans., 1995, **91**, 2751– 2759; b) J. K. Dohrmann and B. Bergmann, J. Phys. Chem., 1995, **99**, 1218– 1227; c) R. E. Hester and K. P. J. Williams, J. Chem. Soc. Faraday Trans. 2, 1982, **78**, 573– 584.
38 This statement is true even when accounting for the systematic overestimation of Fe–L bonds by DFT.
39 a) P. Verma, J. Weir, L. Mirica and T. D. P. Stack, Inorg. Chem., 2011, **50**, 9816– 9825; b) C. G. Pierpont, Inorg. Chem., 2011, **50**, 9766– 9772.
40 a) A. Vlcek, Comments Inorg. Chem., 1994, **16**, 207– 228; b) F. Hartl, D. J. Stufkens and A. Vlcek, Inorg. Chem., 1992, **31**, 1687– 1695; c) F. Hartl and A. VlcekJr, Inorg. Chem., 1996, **35**, 1257– 1265; d) A. E. Baum, S. V. Lindeman and A. T. Fiedler, Chem. Commun., 2013, **49**, 6531– 6533; e) T. J. Dunn, L. Chiang, C. F. Ramogida, M. I. Webb, D. Savard, M. Sakaguchi, T. Ogura, Y. Shimazaki and T. Storr, Dalton Trans., 2012, **41**, 7905– 7914; f) W. J. Barreto, S. R. G. Barreto, R. A. Ando, P. S. Santos, E. DiMauro and T. Jorge, Spectrochim. Acta Part A, 2009, **71**, 1419– 1424; g) Y. Shimazaki, R. Kabe, S. Huth, F. Tani, Y. Naruta and O. Yamauchi, Inorg. Chem., 2007, **46**, 6083– 6090.
41 M. Puranik, J. Chandrasekhar, J. G. Snijders and S. Umapathy, J. Phys. Chem. A, 2001, **105**, 10562– 10569.
42 F. G. Bordwell and J. P. Cheng, J. Am. Chem. Soc., 1991, **113**, 1736– 1743.
43 C. Drouza and A. D. Keramidas, Inorg. Chem., 2008, **47**, 7211– 7224.
44 a) V. Lyaskovskyy and B. de Bruin, ACS Catal., 2012, **2**, 270– 279; b) L. A. Berben, B. de Bruin and A. F. Heyduk, Chem. Commun., 2015, **51**, 1553– 1554; c) O. R. Luca and R. H. Crabtree, Chem. Soc. Rev., 2013, **42**, 1440– 1459; d) V. K. K. Praneeth, M. R. Ringenberg and T. R. Ward, Angew. Chem. Int. Ed., 2012, **51**, 10228– 10234; Angew. Chem., 2012, **124**, 10374; e) P. Chaudhuri, K. Wieghardt, T. Weyhermueller, T. K. Paine, S. Mukherjee and C. Mukherjee, Biol.

Chem., 2005, **386**, 1023– 1033; f) P. Chaudhuri and K. Wieghardt, Prog. Inorg. Chem., 2001, **50**, 151– 216.
45 D. R. Weinberg, C. J. Gagliardi, J. F. Hull, C. F. Murphy, C. A. Kent, B. C. Westlake, A. Paul, D. H. Ess, D. G. McCafferty and T. J. Meyer, Chem. Rev., 2012, **112**, 4016– 4093.
46 J. C. Smart and B. L. Pinsky, J. Am. Chem. Soc., 1980, **102**, 1009– 1015.
47 S. Stoll and A. Schweiger, J. Magn. Reson., 2006, **178**, 42– 55.
48 G. M. Sheldrick, Acta Crystallogr., Sect. A, 2008, **64**, 112– 122.
49 O. V. Dolomanov, L. J. Bourhis, R. J. Gildea, J. A. K. Howard and H. Puschmann, J. Appl. Crystallogr., 2009, **42**, 339– 341.
50 F. Neese, in: ORCA - An Ab Initio, DFT and Semiempirical Electronic Structure Package, version 2.9, Max Planck Institute for Bioinorganic Chemistry, Mülheim, Germany, 2012.
51 a) A. D. Becke, J. Chem. Phys., 1993, **98**, 5648– 5652; b) C. T. Lee, W. T. Yang and R. G. Parr, Phys. Rev. B, 1988, **37**, 785– 789.
52 a) A. D. Becke, J. Chem. Phys., 1986, **84**, 4524– 4529; b) J. P. Perdew, Phys. Rev. B, 1986, **33**, 8822– 8824.
53 a) A. Schafer, C. Huber and R. Ahlrichs, J. Chem. Phys., 1994, **100**, 5829– 5835; b) A. Schafer, H. Horn and R. Ahlrichs, J. Chem. Phys., 1992, **97**, 2571– 2577; c) F. Weigend and R. Ahlrichs, Phys. Chem. Chem. Phys., 2005, **7**, 3297– 3305.
54 a) R. E. Stratmann, G. E. Scuseria and M. J. Frisch, J. Chem. Phys., 1998, **109**, 8218– 8224; b) M. E. Casida, C. Jamorski, K. C. Casida and D. R. Salahub, J. Chem. Phys., 1998, **108**, 4439– 4449; c) R. Bauernschmitt and R. Ahlrichs, Chem. Phys. Lett., 1996, **256**, 454– 464.
55 a) S. Hirata and M. Head-Gordon, Chem. Phys. Lett., 1999, **314**, 291– 299; b) S. Hirata and M. Head-Gordon, Chem. Phys. Lett., 1999, **302**, 375– 382.
56 L. Laaksonen, J. Mol. Graph., 1992, **10**, 33.